AGU ADVANCING EARTH AND SPACE SCIENCE

Geophysical Research Letters

RESEARCH LETTER
10.1029/2020GL089455

Roles of Shear and Convection in Driving Mixing in the Ocean

Gregory N. Ivey[1], Cynthia E. Bluteau[2], Bishakhdatta Gayen[3,4], Nicole L. Jones[1], and Taimoor Sohail[5]

[1]Oceans Graduate School and Oceans Institute, University of Western Australia, Crawley, Australia, [2]Institut des Sciences de la Mer, Université du Québec à Rimouski, Rimouski, Canada, [3]Department of Mechanical Engineering, University of Melbourne, Melbourne, Australia, [4]Centre for Atmospheric Oceanic Sciences, Indian Institute of Science, Bangalore, India, [5]School of Mathematics and Statistics, University of New South Wales, Sydney, Australia

Key Points:

- When $Ri < 0.25$ shear dominates ocean mixing whereas when $Ri > 1.0$ convective mixing dominates
- In the ocean, the maximum Ri_f for shear mixing approaches 0.5, while for convective mixing it approaches 0.75
- We propose a generalized KPP model covering the range $0 < Ri < 2$ which accounts for both shear and convective mixing in the ocean

Correspondence to:
G. N. Ivey,
greg.ivey@uwa.edu.au

Citation:
Ivey, G. N., Bluteau, C. E., Gayen, B., Jones, N. L., & Sohail, T. (2021). Roles of shear and convection in driving mixing in the ocean. *Geophysical Research Letters*, *48*, e2020GL089455. https://doi.org/10.1029/2020GL089455

Received 6 JUL 2020
Accepted 17 NOV 2020

Abstract Using field, numerical, and laboratory studies, we consider the roles of both shear and convection in driving mixing in the interior of the density-stratified ocean. Shear mixing dominates when the Richardson number $Ri < 0.25$, convective mixing dominates when $Ri > 1.0$, and in the intermediate regime when $0.25 < Ri < 1.0$ both shear and convection can contribute to mixing. For pure shear mixing the mixing efficiency Ri_f approaches 0.5, while for pure convective mixing the mixing efficiency Ri_f approaches 0.75. The diapycnal diffusivities for the two mechanisms are given by very different expressions. Despite these complexities, a simple mixing length model using the mean flow shear S provides robust estimates of diffusivity across the range $0 < Ri < 2$. To account for the roles of both shear and convection over this range of Ri, we also formulate a modified version of the empirical KPP model for parameterizing ocean mixing in numerical models.

1. Introduction

Diapycnal mixing in the density-stratified ocean controls the mixing of heat, salt, momentum and passive tracers (e.g., Wunsch & Ferrari, 2004). While there are many models of diapycnal ocean mixing (e.g., Burchard & Petersen, 1999; Large et al., 1994; Mater & Venayagamoorthy, 2014a; Warner et al., 2005; Zaron & Moum, 2009), considerable uncertainty still exists in regard to the accuracy of these models when used in ocean circulation models. Measurements of ocean turbulence in the field thus remain important in testing and developing these mixing models. The key turbulence quantities measured in ocean observations are the rate of dissipation of turbulent kinetic energy ϵ and the rate of dissipation of thermal variance χ. While free-falling turbulence profilers have historically provided the bulk of these measurements (Lueck et al., 2002), more recently moored microstructure timeseries measurements have also been used (Bluteau et al., 2013; Holleman et al., 2016; Ivey et al., 2018; Moum & Nash, 2009). The models proposed by either Osborn (1980) or Osborn and Cox (1972) are then typically used to convert these turbulence measurements into diapycnal mixing rates or diffusivities K_ρ.

The Osborn (1980) model, based on the turbulent kinetic energy equation, assumes that ϵ is produced by the interaction of the vertical turbulent momentum flux with the vertical gradient or shear of the mean horizontal velocity $\overline{u}$. The Osborn and Cox (1972) model, based on the thermal variance equation, assumes that χ is produced by the interaction of the vertical turbulent heat flux with the vertical gradient of the mean temperature $\overline{\theta}$. Turbulence can also be produced in the interior of a stratified fluid by a local convective instability when heavy fluid is locally displaced over lighter fluid, or vice-versa. Thorpe (2018), for example, suggested that small scale internal waves in a continuously stratified fluid can steepen until isopcynals eventually fold over to produce regions of local static instability, subsequently generating local patches of convective instability. Large scale nonlinear internal waves traveling in the thermocline can also generate patches of convective instability within the wave's core when the local fluid velocity in the direction of wave propagation exceeds the wave phase velocity (e.g., Gayen & Sarkar, 2014; Jones et al., 2020; Lamb, 2014; Rayson et al., 2019; Zhang & Alford, 2015). In all these examples, however, there is always some background mean flow shear $S = \mathrm{d}\overline{u} / \mathrm{d}z$ associated with the internal waves that can also contribute to mixing. Thus, none of these internal wave examples are cases of "pure" convective instability.

While preceding work has demonstrated that both shear and convection mechanisms can drive diapycnal mixing in the interior of the ocean, a number of questions remain unresolved: (i) when does either mechanism dominate; (ii) what is the efficiency of mixing; (iii) what is the diapycnal diffusivity for each mechanism; (iv) can the two different mechanisms operate together; and (v) what are the implications for parameterizing ocean mixing? These questions are the focus of the present study.

2. Mixing Mechanisms

To quantify mixing in a density-stratified fluid, Winters et al. (1995) argued one must distinguish between the reversible and irreversible components of mixing. Using this framework, Salehipour and Peltier (2015) generalized a model for the (true) diapycnal diffusivity K_ρ^* (here * refers to irreversible quantities) given by

$$K_\rho^* = \left(\frac{Ri_f^*}{1 - Ri_f^*}\right)\frac{\epsilon}{N_*^2} = \frac{\mathcal{M}}{N_*^2} \tag{1}$$

where the (true) flux Richardson number $Ri_f^* = \mathcal{M} / \left(\mathcal{M} + \epsilon\right)$ (Caulfield & Peltier, 2000) is the local mixing efficiency based on the re-sorted background density and, as seen from the last term in Equation 1, $\mathcal{M}$ represents the irreversible diffusive flux.

While the model in Equation 1 is mechanism agnostic—there is no assumption about the mechanism causing mixing—it requires the ability to obtain a reference state of minimum potential energy by re-sorting the 3D density field. This can be accomplished either by re-sorting the 3D density field at a particular time step (as in a mumerical model), or by using a laboratory experiment with a closed control volume where (after mixing has occurred) the fluid adiabatically re-sorts itself as it comes to rest. As all ocean turbulence measurements are obtained from either a microstructure vertical profile or from moored time series at one location, the model in Equation 1 cannot be used with these turbulence measurements to compute the diffusivity.

2.1. Shear Mixing

The most commonly studied turbulent mixing mechanism in the stratified ocean is that driven by a vertically sheared mean flow. Miles (1961) and Howard (1961) showed that in an inviscid, stably stratified fluid with buoyancy frequency $N = \sqrt{-\left(g / \rho\right)\left(\partial\rho / \partial z\right)}$ subjected to a steady vertical shear $S = \mathrm{d}\overline{u} / \mathrm{d}z$, the flow becomes unstable when the gradient Richardson number $Ri = N^2 / S^2 < 0.25$. Numerous studies have since extended this analysis and shown that, as long as Ri is not too large, shear flows are unstable when there is a viscous-diffusive fluid (Howland et al., 2018), when there is preexisting ambient turbulence in the fluid (Kaminski & Smyth, 2019), or when the shear is unsteady (Radko, 2019).

When $Ri < 0.15$ Venayagamoorthy and Koseff (2016) demonstrated that

$$\frac{\mathcal{M}}{\mathcal{M} + \epsilon} \equiv \frac{B}{B + \epsilon} \tag{2}$$

where B is the buoyancy flux. For $Ri > 0.15$ the estimates on the left and right hand sides of Equation 2 progressively diverge (see Venayagamoorthy & Koseff, 2016 their Figures 1 and 3 for details). However if $Ri < 0.15$, then the true diffusivity can be estimated from the buoyancy flux B, and hence Equation 1 can be simplified to the expression first proposed by Osborn (1980)

$$K_\rho = \left(\frac{Ri_f}{1 - Ri_f}\right)\frac{\epsilon}{N^2} = \frac{B}{N^2} \tag{3}$$

where the flux Richardson number $Ri_f = B/(B + \epsilon)$. The challenge in using Equation 3 is that Ri_f must be independently known, and in practice Ri_f is not constant (e.g., Bluteau et al., 2013; Davis & Monismith, 2011;

Holleman et al., 2016; Ivey et al., 2018; Ijichi & Hibiya, 2018; Salehipour et al., 2015; Shih et al., 2005; Walter et al., 2014). And it has been argued that Ri_f cannot even be expressed as a function of a single dimensionless parameter (e.g., Mater & Venayagamoorthy, 2014b).

This problem of needing to first specify Ri_f is circumvented with the model of Osborn and Cox (1972) who proposed that the vertical diffusivity for heat K_θ can be estimated as

$$K_\theta = \frac{\chi}{2\left(\partial\bar{\theta} \,/\, \partial z\right)^2} \tag{4}$$

If the temperature gradient $\partial\bar{\theta} \,/\, \partial z$ dominates the density gradient, then one can assume that K_θ is equal to K_ρ. Direct numerical simulation (DNS) studies of stratified shear flows have compared K_θ with K_ρ (e.g. Itsweire et al., 1993), and recent simulations have shown that K_θ is within a factor or 2 (either low or high) of K_ρ^* for buoyancy Reynolds numbers $Re_b = \epsilon/(\nu N^2)$ as large as 5×10^4 (Kirkpatrick et al., 2019; Salehipour & Peltier, 2015). Although restricted to cases with $Re_b < 250$, the DNS study of unsheared stratified mixing by Taylor et al. (2019) also found that Equation 4 was a good estimator of K_ρ^*.

A third mixing model, proposed by Odier et al. (2009), is based on a Prandtl mixing length model for a shear flow and is given by

$$K_\rho = L_\rho^2 S \tag{5}$$

When temperature dominates the density gradient, the mixing length scale L_ρ is (Ivey et al., 2018)

$$L_\rho = \left(\frac{\chi}{2S\left(d\bar{\theta} \,/\, dz\right)^2} \right)^{\frac{1}{2}} \tag{6}$$

And with L_ρ now defined, the mixing efficiency Ri_f in Equation 3 can be written as (Ivey et al., 2018)

$$Ri_f = \frac{1}{1+D} = \frac{1}{1+\left[\left(L_O^2 L_S\right) / L_\rho^3\right]^{2/3}} \tag{7}$$

where $L_O = \left(\epsilon \,/\, N^3\right)^{1/2}$ is the Ozmidov length scale and $L_S = \left(\epsilon \,/\, S^3\right)^{1/2}$ is the Corrsin shear length scale. Thus $Ri_f = Ri_f(L_O, L_S, L_\rho)$, and the DNS results of Kirkpatrick et al. (2019) are entirely consistent with Equation 7. As argued by Ivey et al. (2018), D has a lower bound of 1, thus yielding an upper bound of $Ri_f = 0.5$ for shear flows.

Using field and laboratory observations obtained across a range of length scales spanning three orders of magnitude, Ivey et al. (2018), also showed the mixing length scale $L_\rho \approx 0.3 L_E$, where the Ellison length scale $L_E = \tilde{\rho} \,/\, \left(\overline{d\rho \,/\, dz}\right)$. The Ellison scale can be computed from time series measurements and has the advantage of not requiring direct estimates of turbulence quantities such as χ or ϵ from specialized instruments. The Ellison scale does, however, require sampling fast enough to resolve the larger energy containing scales and records that are not influenced by internal waves or mean flows. Equation 5 can thus be approximated by

$$K_\rho = 0.1 L_E^2 S. \tag{8}$$

Almost all numerical studies have focused on shear flows when $Ri < 0.25$ and are unstable with active mixing (e.g., Salehipour & Peltier, 2015; Shih et al., 2005; Smyth et al., 2001). But what happens when $Ri > 0.25$? As we show below, mixing still occurs in both field observations and numerical modeling and we evaluate

the predictive capability of the shear-driven mixing models in Equations 3, 4, and 8 when $Ri > 0.25$. We also determine when the mechanism of convective instability starts to become important.

2.2. Convective Mixing

By convective mixing we refer here to mixing that occurs in the interior of the density-stratified water column due to a local instability in the mean density gradient. This process is distinct from mixing driven by an externally imposed buoyancy flux at the free surface (as considered by Sohail et al., 2018, for example, where processes such as surface cooling, evaporation or salt rejection can occur). A common feature of interior convective mixing observed in either laboratory experiments (Wykes & Dalziel, 2014) or in idealized numerical simulations (Chalamalla & Sarkar, 2015; Gayen & Sarkar, 2011; Puthan et al., 2019) is the often efficient mixing with $Ri_f^* > 0.5$. As discussed above, as internal waves always induce some background vertical velocity shear S, internal wave forcing does not drive pure convective instabilities in the ocean.

A good example of pure convective instability, however, is the laboratory experiments of Barry et al. (2001). They conducted a zero mean shear mixing experiment by horizontally oscillating a vertically oriented square-bar mesh grid in a rectangular tank filled with a density stratified fluid (see their Figure 1). The tank was filled with a linearly salt-stratified fluid, the initial density profile was measured, and the fluid was then continuously agitated by rapidly moving the grid back and forth throughout the entire tank (but without creating any mean flow). Once the grid was stopped, the fluid was allowed to come to rest and the final density profile was then measured. The diffusivity K_ρ^* was calculated from the increase in background potential energy after mixing, and N_* was taken as the average of the two (near-linear) before and after density profiles. The moving grid was instrumented with a force transducer and the dissipation ϵ in the fluid was calculated directly. The experiments varied ϵ, N_*, and fluid viscosity ν but, as $S = 0$, the experiments all had $Ri = N_*^2 / S^2 = \infty$. The buoyancy Reynolds number reached values as large as $Re_b = 10^5$, comparable to the highest values seen in the ocean (e.g., Gargett et al., 1984).

Barry et al. (2001) found from their measurements that the diapycnal diffusivity was given by

$$K_\rho^* = 24\nu^{2/3}\kappa^{1/3}Re_b^{1/3} \tag{9}$$

Barry et al. (2001) also found the largest overturning scales were given by $L_E = 20L_{co}$, where they introduced the convective lengthscale defined as $L_{co} = (\nu\kappa)^{1/4} / N_*^{1/2}$. Hence the Rayleigh number $Ra = N_*^2 L_E^4 / (\nu\kappa) \approx 2 \times 10^5$ in their experiments. The diffusivity in Equation 9 is independent of the large scale shear S which, as noted by Mater and Venayagamoorthy (2014a), is a key difference between pure convective and shear mixing.

While Barry et al. (2001) did not discuss or provide estimates of mixing efficiency Ri_f^*, these can now be calculated from their measurements using the framework proposed by Salehipour and Peltier (2015). In particular, substituting Equation 9 into Equation 1 yields

$$Ri_f^* = \frac{\mathcal{M}}{(\mathcal{M} + \epsilon)} = \frac{1}{1 + (1/24)Pr^{1/3}Re_b^{2/3}} \tag{10}$$

For a fixed Pr, Equation 10 demonstrates that $Ri_f^* = Ri_f^*(L_O, L_K)$, a very different length scale dependence than that found in Equation 7 for a shear flow.

Using Equations 9 and 10, we can estimate the range of Ri_f^* and K_ρ^* for convective mixing in the laboratory experiments and under typical oceanic conditions. As the laboratory experiments of Barry et al. (2001) were salt stratified with $Pr = 700$, at their lower limit of $Re_b = 10$ we obtain $Ri_f^* = 0.37$ from Equation 10 and $K_\rho^* \approx 500\kappa$ from Equation 9. The upper limit for their laboratory experiments was $Re_b = 10^5$ and hence we obtain $Ri_f^* = 0.001$ and $K_\rho^* \approx 10^5\kappa$. For representative ocean conditions of $Pr = 7$ and a lower limit of $Re_b = 10$ (e.g., Ivey et al., 2008), Equation 10 yields $Ri_f^* = 0.73$, while Equation 9 predicts $K_\rho^* \approx 180\kappa$. At a

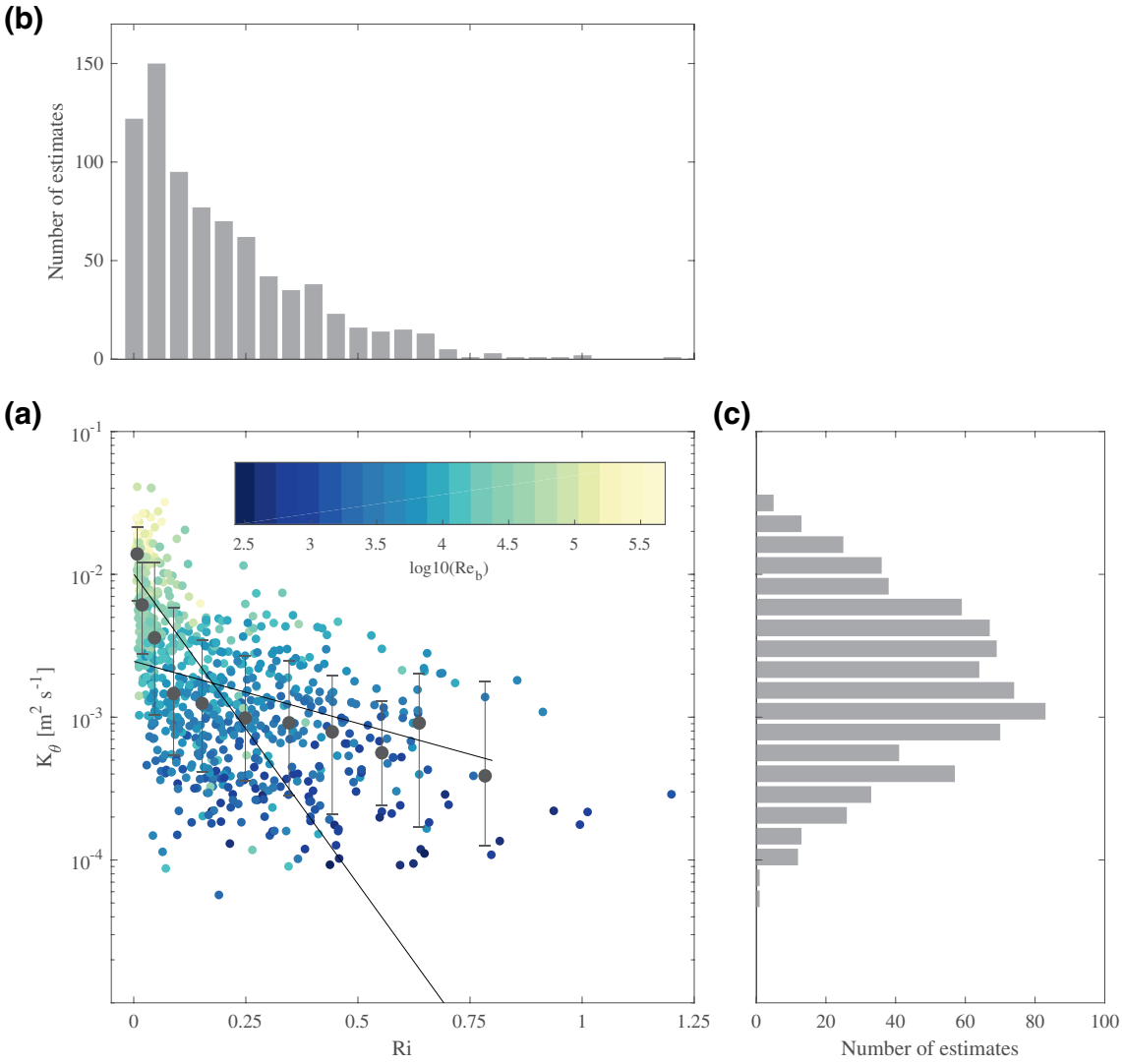

Figure 1. (a) Observed diffusivities K_θ as a function of Ri obtained at the MTPs during the 10 days of measurement. For comparison with the observations, the first line is $K_\rho = (1 \times 10^{-2})e^{-10Ri}$ (399 points, $r^2 = 0.17$) and the second line for Ri > 0.15 is $K_\rho = (2.5 \times 10^{-3})e^{-2Ri}$ (388 points, $r^2 = 0.023$); (b) histogram of estimated *Ri*; and (c) histogram of diffusivities K_θ. The black circles in (a) represent median values of the binned data, with error bars containing 68% of the data in each bin (16th and 84th percentiles). MTP is moored turbulence package.

typical oceanic upper limit of $Re_b = 10^5$ (e.g., Gargett et al., 1984), Equations 10 and 9 predict $Ri_f^* = 0.006$ and $K_\rho^* \approx 5 \times 10^3 \kappa$, respectively. Equations 9 and 10 thus predict wide ranges in mixing efficiencies and diffusivities resulting from convective mixing in the ocean.

2.3. Mixing Mechanisms in the Ocean

The shear and convective mixing mechanisms discussed above are thus quite different, as shown by the differing expressions for both the mixing efficiencies in Equation 7 versus Equation 10 and the diffusivities in Equation 3 versus Equation 9. The diffusivity in Equation 9 is derived from a laboratory experiment with zero mean shear and hence *Ri* is infinite, but in the ocean there is inevitably some shear and so *Ri* will almost always be finite. Are the diffusivities observed in the ocean therefore ever consistent with the prediction for pure convective mixing given by Equation 9? Can convective mixing ever dominate ocean mixing? When does

shear mixing dominate ocean mixing? Can the two mechanisms operate together? To address these questions, we examine below two sources of information: field observations collected on the Australian North West Shelf (NWS) and numerical simulations of an oscillating stratified flow over a smooth bottom.

3. Data Sources

3.1. Field Observations

The field observations come from a 34 m long mooring bottom-anchored on the NWS in 105 m of water. The site is energized by strong and nonlinear internal tidal motions on the NWS. Details of the measurements are given in Bluteau et al. (2016a), but briefly the mooring was deployed from 4–22 April 2012 and was instrumented with: (i) 22 temperature sensors (including Seabird Electronics SBE56 and SBE39 sensors) sampling respectively at 0.5 and 10 s; (ii) a conductivity-temperature sensor (Seabird Electronics, SBE37) sampling at 15 s; (iii) a temperature-pressure sensor sampling at 10 s (SBE39, Sea-Bird Electronics); and (iv) an upward-looking 300 kHz acoustic-Doppler current profiler (ADCP, RDInstruments) measuring velocities in 1 m bins over 1-min averages (see Table 1 of Bluteau et al., 2016b). The SBE56 thermistors were vertically spaced at 0.75 m around the moored turbulence packages (MTPs), and 1 m elsewhere on the mooring. As detailed by Ivey et al. (2018), these velocity, temperature, and salinity observations were used to estimate the background shear S and stratification N around the heights of the MTPs described below using the same segment length of 8.53 min as the turbulence computations, corresponding to a time-scale of approximately half the time-mean buoyancy period.

Two MTPs were placed on the mooring at 7.5 and 20.5 m above the seabed (ASB) to provide estimates of ϵ and χ, using the observations from an acoustic-Doppler velocimeter (ADV, Vector, Nortek-AS) and a fast-response temperature sensor (FP07, GE Thermometics). The MTPs recorded data for the first 10 days of the deployment. To ascertain whether the MTPs were in the bottom boundary layer, we compared the Ellison length scale $L_E = \tilde{\theta} / \left(\partial\overline{\theta} / \partial z\right)$ (computed over the same time- and length-scales as the other turbulence and mean quantities [e.g., N and S]) to the log law of the wall integral scale $L_z = kz$, where k is von Karmans constant. Estimates with $L_E > L_z$ were removed from further analysis, leaving us with observations of the density stratified fluid at a depth of around 100 m, but free from any surface or bottom influence. Each MTP included a motion pack to recover the instruments' motion and correct the velocity spectral observations using the techniques described by Bluteau et al. (2016b). We fitted the ADV and FP07 spectral observations (computed with 8.53 min segments) over their respective inertial subranges to yield estimates ϵ and hence χ using the inertial subrange fitting methods described by Bluteau et al. (2011, 2017). With χ determined, the diffusivity K_θ was then determined from Equation 4. Whether the mixing mechanism is shear or convective in nature, for the reasons discussed above in Section 2.1 we assume that K_θ is a good estimator of $K_\rho{}^*$.

3.2. Numerical Simulations

Using resolved large eddy simulations (LES), Gayen et al. (2010) considered an initially linearly stratified oscillating tidal flow over a flat bottom. Their simulations solved the three-dimensional unsteady Navier-Stokes equations under the Boussinesq approximation. An initially linear ambient stratification was imposed in the vertical direction and the unsteady free-stream velocity U was forced by an oscillating pressure gradient in the horizontal direction, thus modeling the forcing by a semi-diurnal tidal flow with frequency ω. Detailed descriptions of the solution technique and model setup are found in Gayen et al. (2010). The large scale Reynolds number $Re_S = U^2/\omega\nu = 1790$ (where U is the unsheared free-stream velocity and ω the tidal frequency) and the bulk Richardson number $Ri_b = N^2/\omega^2 = 500$, which Gayen et al. (2010) considered a moderate stratified case. While their original simulations were done with $Pr = 0.7$, the results discussed here were achieved with a new simulation with $Pr = 7$ to better represent ocean conditions.

We chose a computational grid with an effective grid resolution in the mean flow direction of $x^+ = (xu_*/\nu) = 60$ (where u_* was the bottom friction velocity) and in the cross flow direction of $y^+ = (yu_*/\nu) = 30$. The horizontal grid resolution in both the mean and transverse flow directions was uniform throughout the domain. In the vertical direction, a variable grid resolution was used with strong clustering near the bottom with

$z^+ = (zu_*/\nu) = 2$ to resolve the viscous sublayer. This resolution was sufficient to resolve the near-wall eddies that carry the Reynolds stress. Far from the bottom in the weakly sheared interior the vertical grid scale was relaxed to $z^+ = (zu_*/\nu) = 20$. As discussed in Gayen et al. (2010), our numerical simulation thus resolved the flow near the bottom and did not require any near-wall closure model. A dynamic eddy viscosity and eddy diffusivity model was used for subgrid scale closure well away from the bottom in the interior.

After just one tidal cycle, the flow started to form a three-layer structure (see Figure 1a of Gayen et al., 2010). The three-layer structure consisted of a strongly sheared (but nearly well-mixed layer) bottom layer of height h_m, a second weakly sheared (but linearly stratified) region in the interior, and a third relatively thin (and strongly sheared) pycnocline region separating the bottom layer from the linearly stratified interior. The height of the bottom mixing layer h_m was defined as the height where the local density gradient first reached 0.1 of the interior density gradient. The gradient Richardson number Ri was generally very small near the bottom and increased with height. The height above the bottom where Ri first reached 0.25 was defined as $h_{0.25}$ (Gayen et al., 2010 found $h_m \approx 0.9h_{0.25}$), and the value of Ri then continued to increase with height above $h_{0.25}$. A classical logarithmic mean velocity profile was only seen during a small portion of the tidal cycle. All mixing estimates were calculated once the simulation had reached a statistical steady state, which took about 10–12 tidal cycles. Over the next five tidal cycles, all mean and turbulence properties at a particular instant and height were horizontally averaged in the (x, y) plane, a spatial averaging process denoted by <>. Data were taken in the vertical over the range $z^+ = 200 - 800$. The Ellison scale was calculated as $L_E = < \tilde{\rho} / (\mathrm{d}\rho / \mathrm{d}z) >$ and the vertical eddy diffusivity was calculated using two methods. First, to allow direct comparison with the analysis methods used in processing the field data above, we calculated the diffusivity from the buoyancy flux B as $K_\rho = <B / N^2>$. Second, we re-sorted the instantaneous density fields to get the irreversible diffusive flux $\mathcal{M}$ and hence also calculated $K_\rho^* = \mathcal{M} / N^2$.

4. Results

4.1. Field Observations

The values of both Ri and K_θ varied strongly during the 10 days over which the MTPs collected turbulence observations (Figure 1). Around 65% of the data had $Ri < 0.25$ and 95% of the data had Ri less than 0.6 (Figure 1b). Around 90% of the events had diffusivities K_θ between 10^{-4} m^2 s^{-1} and 10^{-2} m^2 s^{-1} (Figure 1c). The largest Ri observed was $Ri \approx 1.25$, but mixing events with such large values of Ri were rare. For $Ri < 0.02$ bin-averaged diffusivities $K_\theta > 10^{-2}$ m^{2}s^{-1} and in this limit the observations had $Re_b > 10^5$ (Figure 1a). As Ri increased, the diffusivities then progressively decreased with increasing Ri (Figure 1a). Zaron and Moum (2009) suggested a modified version of the original KPP model of Large et al. (1994), where this decay was exponential with Ri with an exponent of −10. As shown in Figure 1a, this appears a reasonable description for small $Ri < 0.15$, but for most of the Ri range a lower value for the exponent is required, and the second line shown for comparison in Figure 1a) has an exponent of −2. This choice of exponents is motivated by the numerical results discussed below.

In Figure 2a we compare these observed diffusivities K_θ with the predicted diffusivities for the mixing length model in Equation 8. While individual data points are scattered, once binned the observations are consistent with the predictions within the error bounds shown over the observed range of Ri. In Figure 2b we compare these observed diffusivities with the predictions for convective mixing in Equation 9. For Ri close to 0, Equation 9 clearly underpredicts the observed K_θ, but as Ri increases the binned observations approach the predicted value for convectively dominated mixing. The challenge is there are very few estimates in the field data with $Ri > 0.75$, reflecting the practical difficulty of making reliable estimates of the mean velocity gradients to accurately estimate high Ri values in the field. This constraint with the available field data is one motivation for examining independent data from a numerical model, as discussed below.

4.2. Numerical Simulations

The results of the numerical simulations are shown in Figure 3. Overall around 85% of the data have $Ri < 0.25$ while only 15% have $Ri > 0.25$. The points with $Ri > 0.25$ typically correspond to times when

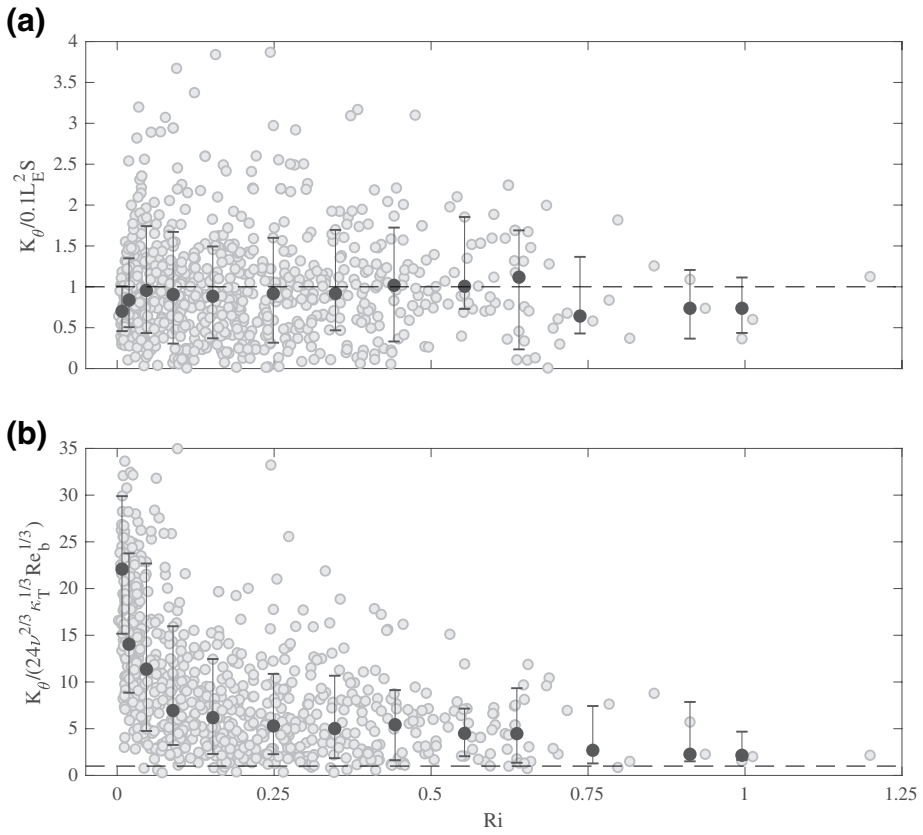

Figure 2. Observed diffusivities K_θ as a function of Ri where we nondimensionalize K_θ with: (a) the predicted diffusivity from the mixing length model in Equation 8; and (b) the predicted diffusivity from the convective mixing model in Equation 9. The black circles represent median values of the binned data with error bars containing 68% of the data in each bin (16th and 84th percentiles).

the oscillating flow was reversing and the vertical shear S was small. In Figure 3a, we plot K_ρ versus Ri and in Figure 3b we plot K_ρ^* versus Ri. What is striking is that K_ρ appears a very good representation of K_ρ^*. For very low Ri, both diffusivities approach 10^{-4} m^{2}s^{-1}. As Ri increases, both diffusivities decrease progressively toward 10^{-6} m^{2}s^{-1} as Ri approaches 2. Also shown in Figures 3a and 3b, are exponential decay lines for the diffusivities as a function of Ri. Consistent with the field data, an exponential decay with an exponent of -10 is reasonable only for small Ri. For $0.15 < Ri < 2$ a much smaller exponent is clearly required, and for comparison we show a line with an exponent of -2. This is a simple first suggestion and clearly more data is required, particularly in the regime where $Ri > 1.25$. In summary, the field observations (Figure 2a) and the numerical simulations (Figure 3b) thus show a very similar decrease of diffusivity with increasing Ri, although the numerical results extend to much higher Ri than the field observations.

Given the very similar dependence of K_ρ and K_ρ^* with Ri in Figures 3a and 3b, we restrict our analysis to K_ρ in the remaining panels. In Figures 3c and 3d, we compare the diffusivities K_ρ from the simulations with those predicted from the same two mixing models evaluated above with the field observations. The predictions from the mixing length model in Equation 8 are in good agreement with the numerical diffusivities out to the observed upper bound of $Ri = 2$ (Figure 3c). Figure 3d compares the simulation diffusivities K_ρ with the predicted diffusivities for convective mixing in Equation 9. For small Ri, the convective model underestimates the diffusivities by as much as a factor of 5. When $Ri > 1$, however, more than 80% of the diffusivities are within a factor of 0.5 (high or low) of the predictions of the convective model in Equation 9.

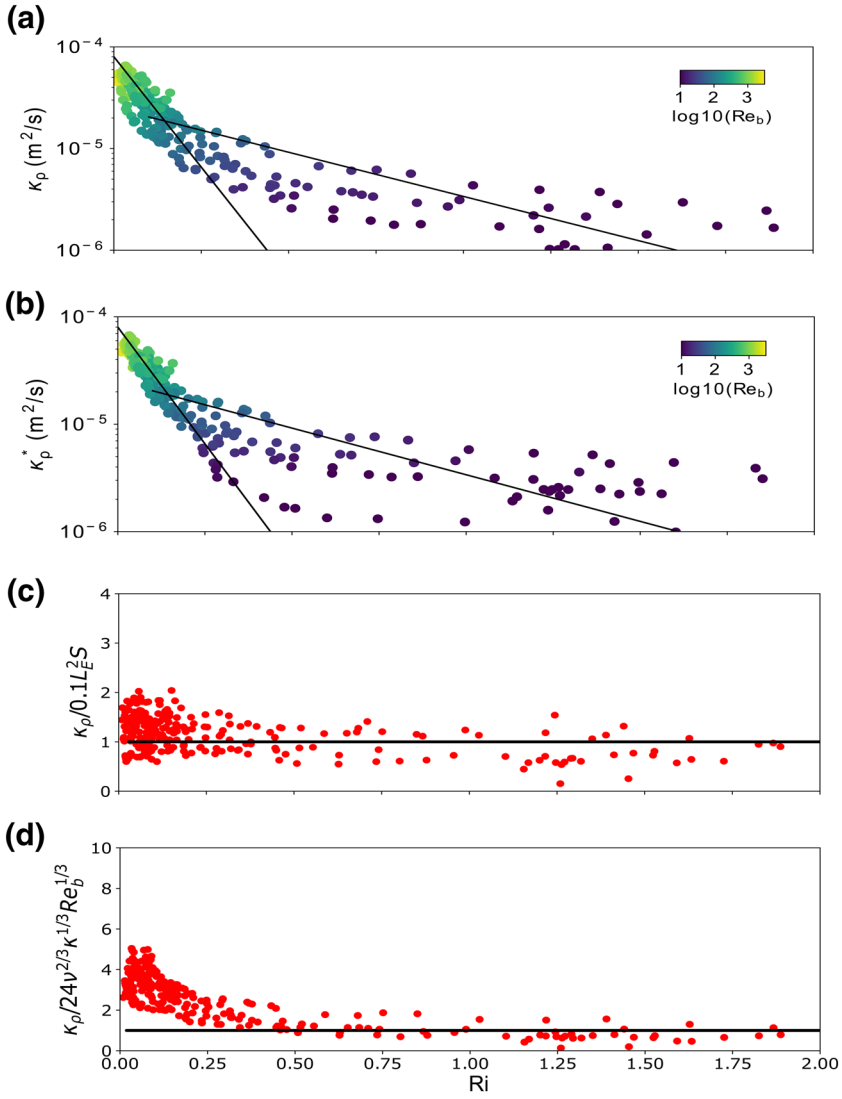

Figure 3. Diffusivities from the LES simulations as a function of *Ri*. (a) K_ρ versus *Ri*. The line shown for the interval $0 < Ri < 0.15$ is $K_\rho = (8 \times 10^{-5})e^{-10Ri}$ (1,300 points and $r^2 = 0.56$). The line shown for the interval $0.15 < Ri < 2$ is $K_\rho = (2.5 \times 10^{-5})e^{-2Ri}$ (200 points and $r^2 = 0.4$); (b) K_ρ^* vs. *Ri*, and the lines shown are as in (a); (c) K_ρ nondimensionalized with the predicted diffusivity from the mixing length model in Equation 8; and (d) K_ρ nondimensionalized by the predicted diffusivity from the convective mixing model in Equation 9. LES is large eddy simulations.

5. Discussion and Conclusions

The field observations and the numerical simulations are very consistent in demonstrating that the Richardson number *Ri* provides a useful differentiation between the shear and convective mixing mechanisms (from hereon we drop the superscript * for simplicity of notation). Our results show that when $Ri < 0.25$, the mixing is dominated by shear, the mixing efficiency $Ri_f = Ri_f(L_O, L_S, L_\rho)$, and Ri_f is in the range from 0 to 0.5. When $Ri > 1.0$, the mixing is dominated by convection, the mixing efficiency $Ri_f = Ri_f(L_O, L_K)$, and Ri_f is in the range from 0 to 0.75. In the intermediate case when $0.25 < Ri < 1.0$, our results imply that both the shear and convective mechanisms can contribute to mixing.

The field and numerical results both show there is a progressive two order of magnitude decrease in K_ρ as *Ri* increases from 0 to 2. However, the field and numerical results show that K_ρ is not determined solely by *Ri*: at the same value of *Ri*, the field values of K_ρ are nearly two orders of magnitude larger. For both the shear

and convective mechanisms Ri appears as a natural and important parameter or, since $Ri = \left(L_S / L_O\right)^{4/3}$, both the Corrsin length scale L_S and the Ozmidov length scale L_O are important. But the Kolmogorov scale L_K characterizing the smallest scales is also important in any turbulent flow, and three length scales imply a second dimensionless parameter is necessary. An obvious choice for this parameter is $Re_b = \left(L_O / L_K\right)^{4/3}$. There is a factor of 10^2 difference in the Re_b between the field observations in Figure 1 and the numerical results in Figure 3. The much higher value of Re_b in the field seems the likely cause for the difference in the magnitude of K_ρ for the same Ri.

Our analysis shows that while Ri is a useful parameter in distinguishing between shear and convective mixing, Ri alone cannot be used to predict diffusivity in the ocean. The popular KPP closure model of Large et al. (1994) makes four assumptions: mixing only occurs due to shear; K_ρ depends only on Ri; in the limit when $Ri \to 0$ the diffusivity $K_\rho \to K_0 = 5 \times 10^{-3} \mathrm{m^2 s^{-1}}$; and when $Ri > 0.7$ the diffusivity $K_\rho = 0$. None of these assumptions are supported by our results.

Our results can, however, be used to formulate a modified version of the KPP model similar to that suggested by Large et al. (1994) (a decaying polynomial dependence on Ri) and Zaron and Moum (2009) (a decaying exponential dependence on Ri). Consistent with both the field and numerical results presented here, the following empirical expression accounts for both shear and convective mixing over a wide range of Ri

$$\begin{aligned} Ri < 0.15 \quad & K_\rho = K_0 \exp^{-(10Ri)} \\ 0.15 < Ri < 2 \quad & K_\rho = 0.3K_0 \exp^{-(2Ri)} \\ & K_0 = \left(1 \times 10^{-7}\right) Re_{b0} \end{aligned} \tag{11}$$

where Re_{b0} is the buoyancy Reynolds number in the limit when $Ri \to 0$. For the field data, $Re_{b0} \approx 10^5$ and $K_0 \approx 10^{-2}$ $\mathrm{m^2 s^{-1}}$ (Figure 1b)—only a factor of 2 above the K_0 value proposed by Large et al. (1994)—while for the numerical data $Re_{b0} \approx 10^3$ and $K_0 \approx 8 \times 10^{-5}$ $\mathrm{m^2 s^{-1}}$ (Figure 3a). Equation 11 requires as input a value of Re_{b0} in order to determine K_0. As a first step, we propose adopting the same $K_0 = 5 \times 10^{-3}$ $\mathrm{m^2 s^{-1}}$ suggested by Large et al. (1994) and then using Equation 11 over the full range of the computed Ri. The exponent of −10 is reasonable only for $Ri < 0.15$ and a lower exponent is needed as Ri increases. There are few data points at large Ri and the exponent of −2 is just a first suggestion and clearly more data, particularly at $Ri > 1.25$, is required to refine this estimate. And more generally, our proposed formulation in Equation 11 needs to be tested further with measurements of K_0 and estimates of Re_{b0} before use in modeling applications.

The simple mixing length model in Equation 8 appears to be a reliable predictor of the observed diffusivities K_ρ in both the field observations and the numerical results reported here. In practice, this agreement occurs over a broader range of Ri than might be anticipated from mixing length theory, and even appears to be a good predictor of mixing at high Ri when mixing is dominated by convection. Whether the mechanism driving the mixing is shear or convection and irrespective of the value of Ri, it appears Equation 8 can be applied to mooring data to get long time estimates of K_ρ. Such long-term estimates of K_ρ would be invaluable in evaluating the description of mixing within circulation models.

Acknowledgments
Gregory N. Ivey, Cynthia E. Bluteau, and Nicole L. Jones acknowledge the support of the Australian Research Council (DP 180101736). Cynthia E. Bluteau's salary was supported by the Natural Sciences and Engineering Research Council of Canada through a Postdoctoral Fellowship. Bishakhdatta Gayen was supported by the Australian Research Council (ARC) Future Fellowship (FT180100037). Numerical simulations were conducted on the Australian National Computational Infrastructure (NCI, ANU) supported by the Commonwealth of Australia. Our thanks to two anonymous reviewers for helpful comments and feedback on the original manuscript.

Data Availability Statement

The data used in creating the figures are available in a repository for the numerical simulations (http://doi.org/10.5281/zenodo.3819339) and the field observations (http://doi.org/10.5281/zenodo.3840536).

References

Barry, M. E., Ivey, G. N., Winters, K. B., & Imberger, J. (2001). Measurements of diapycnal diffusivities in stratified fluids. *Journal of Fluid Mechanics*, *442*(1), 267–291. https://doi.org/10.1017/S0022112001005080

Bluteau, C. E., Jones, N. L., & Ivey, G. N. (2011). Estimating turbulent kinetic energy dissipation using the inertial subrange method in environmental flows. *Limnology and Oceanography: Methods*, *9*, 302–321. https://doi.org/10.4319/lom.2011.9.302

Bluteau, C. E., Jones, N. L., & Ivey, G. N. (2013). Turbulent mixing efficiency at an energetic ocean site. *Journal of Geophysical Research: Oceans*, *118*(9), 4662–4672. https://doi.org/10.1002/jgrc.20292

Bluteau, C. E., Jones, N. L., & Ivey, G. N. (2016a). Estimating turbulent dissipation from microstructure shear measurements using maximum likelihood spectral fitting over the inertial and viscous subranges. *Journal of Atmospheric and Oceanic Technology*, *116*, 713–722. https://doi.org/10.1175/JTECH-D-15-0218.1

Bluteau, C. E., Jones, N. L., & Ivey, G. N. (2016b). Acquiring long-term turbulence measurements from moored platforms impacted by motion. *Journal of Atmospheric and Oceanic Technology*, *33*(11), 2535–2551. https://doi.org/10.1175/JTECH-D-16-0041.1

Bluteau, C. E., Lueck, R. G., Ivey, G., Jones, N., Book, J., & Rice, A. (2017). Determining mixing rates from concurrent temperature and velocity measurements. *Journal of Atmospheric and Oceanic Technology*, *34*(10), 2283–2293. https://doi.org/10.1175/JTECH-D-16-0250.1

Burchard, H., & Petersen, O. (1999). Models of turbulence in the marine environment–a comparative study of two-equation turbulence models. *Journal of Marine Systems*, *21*(1–4), 29–53. https://doi.org/10.1016/S0924-7963(99)00004-4

Caulfield, C., & Peltier, W. (2000). The anatomy of the mixing transition in homogeneous and stratified free shear layers. *Journal of Fluid Mechanics*, *413*, 1–47. https://doi.org/10.1017/S0022112000008284

Chalamalla, V. K., & Sarkar, S. (2015). Mixing, dissipation rate, and their overturn-based estimates in a near-bottom turbulent flow driven by internal tides. *Journal of Physical Oceanography*, *45*(8), 1969–1987. https://doi.org/10.1175/JP0-D-14-0057.1

Davis, K. A., & Monismith, S. G. (2011). The modification of bottom boundary layer turbulence and mixing by internal waves shoaling on a barrier reef. *Journal of Physical Oceanography*, *41*(11), 2223–2241. https://doi.org/10.1175/2011JP04344.1

Gargett, A. E., Osborn, T. R., & Nasmyth, P. W. (1984). Local isotropy and the decay of turbulence in a stratified fluid. *Journal of Fluid Mechanics*, *144*, 231–280. https://doi.org/10.1017/S0022112084001592

Gayen, B., & Sarkar, S. (2011). Boundary mixing by density overturns in an internal tidal beam. *Geophysical Research Letters*, *38*(14), 48–79. https//doi.org/10.1029/2011GL048135

Gayen, B., & Sarkar, S. (2014). Psi to turbulence during internal wave beam refraction through the upper ocean pycnocline. *Geophysical Research Letters*, *41*(24), 8953–8960. https//doi.org/10.1002/2014GL061226

Gayen, B., Sarkar, S., & Taylor, J. R. (2010). Large eddy simulation of a stratified boundary layer under an oscillatory current. *Journal of Fluid Mechanics*, *643*, 233–266.

Holleman, R. C., Geyer, W. R., & Ralston, D. K. (2016). Stratified turbulence and mixing efficiency in a salt wedge estuary. *Journal of Physical Oceanography*, *46*(6), 1769–1783. https://doi.org/10.1175/JP0-D-15-0193.1

Howard, L. N. (1961). Note on a paper of John W. Miles. *Journal of Fluid Mechanics*, *10*(4), 509–512. https://doi.org/10.1017/S0022112061000317

Howland, C. J., Taylor, J. R., & Caulfield, C. P. (2018). Testing linear marginal stability in stratified shear layers. *Journal of Fluid Mechanics*, *839*, R4. https://doi.org/10.1017/jfm.2018.79

Ijichi, T., & Hibiya, T. (2018). Observed variations in turbulent mixing efficiency in the deep ocean. *Journal of Physical Oceanography*, *48*(8), 1815–1830. https://doi.org/10.1175/JP0-D-17-0275.1

Itsweire, E. C., Koseff, J. R., Briggs, D. A., & Ferziger, J. H. (1993). Turbulence in stratified shear flows: Implications for interpreting shear-induced mixing in the ocean. *Journal of Physical Oceanography*, *23*(7), 1508–1522. https://doi.org/10.1175/1520-0485(1993)023<1508:TISSFI>2.0.C0;2

Ivey, G. N., Bluteau, C. E., & Jones, N. L. (2018). Quantifying diapycnal mixing in an energetic ocean. *Journal of Geophysical Research*, *123*(1), 346–357. https://doi.org/10.1002/2017JC013242

Ivey, G. N., Winters, K. B., & Koseff, J. R. (2008). Density stratification, turbulence, but how much mixing? *Annual Review of Fluid Mechanics*, *40*, 169–184. https://doi.org/10.1146/annurev.fluid.39.050905.110314

Jones, N., Ivey, G., Rayson, M., & Kelly, S. (2020). Mixing driven by breaking nonlinear internal waves. *Geophysical Research Letters*, *47*(19), e2020GL089591. https//doi.org/10.1029/2020GL088499

Kaminski, A., & Smyth, W. (2019). Stratified shear instability in a field of pre-existing turbulence. *Journal of Fluid Mechanics*, *862*, 639–658.

Kirkpatrick, M. P., Williamson, N., Armfield, S., & Zecevic, V. (2019). Evolution of thermally stratified turbulent open channel flow after removal of the heat source. *Journal of Fluid Mechanics*, *876*, 356–412.

Lamb, K. G. (2014). Internal wave breaking and dissipation mechanisms on the continental slope/shelf. *Annual Review of Fluid Mechanics*, *46*, 231–254.

Large, W. G., McWilliams, J. C., & Doney, S. C. (1994). Oceanic vertical mixing: A review and a model with a nonlocal boundary layer parameterization. *Reviews of Geophysics*, *32*(4), 363–403. https://doi.org/10.1029/94RG01872

Lueck, R. G., Wolk, F., & Yamazaki, H. (2002). Oceanic velocity microstructure measurements in the 20th century. *Journal of Oceanography*, *58*(1), 153–174. https://doi.org/10.1023/A:1015837020019

Mater, B. D., & Venayagamoorthy, S. K. (2014a). A unifying framework for parameterizing stably stratified shear-flow turbulence. *Physics of Fluids*, *26*(036601), 3. https://doi.org/10.1063/1.4868142

Mater, B. D., & Venayagamoorthy, S. K. (2014b). The quest for an unambiguous parameterization of mixing efficiency in stably stratified geophysical flows. *Geophysical Research Letters*, *41*(13), 4646–4653. https://doi.org/10.1002/2014GL060571

Miles, J. W. (1961). On the stability of heterogeneous shear flows. *Journal of Fluid Mechanics*, *10*(4), 496–508. https://doi.org/10.1017/S0022112061000305

Moum, J. N., & Nash, J. D. (2009). Mixing measurements on an equatorial ocean mooring. *Journal of Atmospheric and Oceanic Technology*, *26*(2), 317–336. https://doi.org/10.1175/2008JTECH0617.1

Odier, P., Chen, J., Rivera, M., & Ecke, R. (2009). Fluid mixing in stratified gravity currents: The Prandtl mixing length. *Physical Review Letters*, *102*(13), 134. https://doi.org/10.1103/PhysRevLett.102.134504

Osborn, T. R. (1980). Estimates of the local rate of vertical diffusion from dissipation measurements. *Journal of Physical Oceanography*, *10*(1), 83–89. https://doi.org/10.1175/1520-0485(1980)010<0083:EOTLRO>2.0.CO;2

Osborn, T. R., & Cox, C. S. (1972). Oceanic fine structure. *Geophysical Fluid Dynamics*, *3*(1), 321–345. https://doi.org/10.1080/03091927208236085

Puthan, P., Jalali, M., Chalamalla, V. K., & Sarkar, S. (2019). Energetics and mixing in buoyancy-driven near-bottom stratified flow. *Journal of Fluid Mechanics*, *869*, 214–237.

Radko, T. (2019). Instabilities of a time-dependent shear flow. *Journal of Physical Oceanography*, *49*(9), 2377–2392.

Rayson, M. D., Jones, N. L., & Ivey, G. N. (2019). Observations of large-amplitude mode-2 nonlinear internal waves on the Australian north west shelf. *Journal of Physical Oceanography*, *49*(1), 309–328.

Salehipour, H., & Peltier, W. (2015). Diapycnal diffusivity, turbulent Prandtl number and mixing efficiency in Boussinesq stratified turbulence. *Journal of Fluid Mechanics*, *775*, 464–500. https://doi.org/10.1017/jfm.2015.305

Salehipour, H., Peltier, W., & Mashayek, A. (2015). Turbulent diapycnal mixing in stratified shear flows: The influence of Prandtl number on mixing efficiency and transition at high Reynolds number. *Journal of Fluid Mechanics*, *773*, 178–223. https://doi.org/10.1017/jfm.2015.225

Shih, L. H., Koseff, J. R., Ivey, G. N., & Ferziger, J. H. (2005). Parameterization of turbulent fluxes and scales using homogeneous sheared stably stratified turbulence simulations. *Journal of Fluid Mechanics*, *525*, 193–214. https://doi.org/10.1017/S0022112004002587

Smyth, W. D., Moum, J. N., & Caldwell, D. R. (2001). The efficiency of mixing in turbulent patches: Inferences from direct simulations and microstructure observations. *Journal of Physical Oceanography*, *31*(8), 1969–1992. https://doi.org/10.1175/1520-0485(2001)031<1969:TE0MIT>2.0.C0;2

Sohail, T., Gayen, B., & Hogg, A. M. (2018). Convection enhances mixing in the southern ocean. *Geophysical Research Letters*, *45*(9), 4198–4207. https//doi.org/10.1029/2018GL077711

Taylor, J., de Bruyn Kops, S., Caulfield, C., & Linden, P. (2019). Testing the assumptions underlying ocean mixing methodologies using direct numerical simulations. *Journal of Physical Oceanography*, *49*(11), 2761–2779.

Thorpe, S. A. (2018). Models of energy loss from internal waves breaking in the ocean. *Journal of Fluid Mechanics*, *836*, 72–116. https://doi.org/10.1017/jfm.2017.780

Venayagamoorthy, S. K., & Koseff, J. R. (2016). On the flux Richardson number in stably stratified turbulence. *Journal of Fluid Mechanics*, *798*, R1-1–R1-10. https://doi.org/10.1017/jfm.2016.340

Walter, R. K., Squibb, M. E., Woodson, C. B., Koseff, J. R., & Monismith, S. G. (2014). Stratified turbulence in the nearshore coastal ocean: Dynamics and evolution in the presence of internal bores. *Journal of Geophysical Research*, *119*(12), 8709–8730. https://doi.org/10.1002/2014JC010396

Warner, J. C., Sherwood, C. R., Arango, H. G., & Signell, R. P. (2005). Performance of four turbulence closure models implemented using a generic length scale method. *Ocean Modelling*, *8*(1), 81–113. https://doi.org/10.1016/j.ocemod.2003.12.003

Winters, K. B., Lombard, P. N., Riley, J. J., & D'Asaro, E. A. (1995). Available potential energy and mixing in density-stratified fluids. *Journal of Fluid Mechanics*, *289*, 115128.

Wunsch, C., & Ferrari, R. (2004). Vertical mixing, energy, and the general circulation of the oceans. *Annual Review of Fluid Mechanics*, *36*(1), 281–314. https://doi.org/10.1146/annurev.fluid.36.050802.122121

Wykes, M. S. D., & Dalziel, S. B. (2014). Efficient mixing in stratified flows: Experimental study of a Rayleigh-Taylor unstable interface within an otherwise stable stratification. *Journal of Fluid Mechanics*, *756*, 1027–1057.

Zaron, E. D., & Moum, J. N. (2009). A new look at Richardson number mixing schemes for equatorial ocean modeling. *Journal of Physical Oceanography*, *39*(10), 2652–2664.

Zhang, S., & Alford, M. H. (2015). Instabilities in nonlinear internal waves on the Washington continental shelf. *Journal of Geophysical Research: Oceans*, *120*(7), 5272–5283. https://doi.org/10.1002/2014JC010638